Article

Not peer-reviewed version

An Archaeometric Study of the Porcelain Chinese Sherds Found at the Santana Convent in Lisbon – Part 2 – A Comparison with Coeval Chinese Samples of Well-Known Provenance

Luis F. Vieira Ferreira *, Ana Maria Rego, Rosa Varela Gomes, Mário Varela Gomes, Shanshan Li, Manuel F. C. Pereira

Posted Date: 20 May 2026

doi: 10.20944/preprints202605.1370.v1

Keywords: Chinese Porcelains; Santana convent; blue and white glazes; micro-Raman; XPS; GSDR; XRD; XRF; SM

 doi:10.20944/preprints202605.1370.v1

Article

An Archaeometric Study of the Porcelain Chinese Sherds Found at the Santana Convent in Lisbon – Part 2 – A Comparison with Coeval Chinese Samples of Well-Known Provenance

Luís F. Vieira Ferreira [1,*], Ana Maria Rego [1] and Rosa Varela Gomes [2], Mário Varela Gomes [2], Shanshan Li [2,3] and Manuel F. C. Pereira [4]

[1] iBB-Institute for Bioengineering and Biosciences and Associate Laboratory i4HB—Institute for Health and Bioeconomy, and DEQ-Departamento de Engenharia Química at Instituto Superior Técnico, Universidade de Lisboa, 1049-001 Lisboa, Portugal

[2] NOVA/FCSH – Instituto de Arqueologia e Paleociências/História, Territórios e Comunidades-CFE. Departamento de História, Avenida de Berna 26-C, 1069-061 Lisboa, Portugal.

[3] Department of History, Sun Yatsen University, China

[4] CERENA—Centro de Estudos em Recursos Naturais e Ambiente, Instituto Superior Técnico,Universidade de Lisboa, 1049-001 Lisboa, Portugal

* Correspondence: lfvieiraferreira@tecnico.ulisboa.pt

Abstract

Fifteen blue-and-white Chinese porcelain sherds dated from the seventeenth to nineteenth centuries, from Jingdezhen, Anxi, and Dehua kilns, were analysed and compared with fragments recovered from the Santana Convent in Lisbon. This work focuses on the identification of cobalt pigment sources, glaze technology and microstructural features for provenance assessment. Sherds were studied using several non-invasive spectroscopies, namely micro-Raman, X-Ray Photoelectron spectroscopy (XPS), X-Ray Fluorescence (XRF) and Ground State Diffuse Reflectance (GSDR). The mineralogical characterization of the ceramic bodies was performed with the use of the X-ray diffraction technique (XRD) and stereomicroscopy (SM). The GSDR absorption spectra of the dark blue and light blue glazes are in most cases quite different. These spectra, together with the XPS studies point to different forms of cobalt ions emplacement in the surface glassy structure of the glaze, or to the use of different pigments to obtain the dark or the light blues decoration of the porcelains. This study aims to clarify the provenance of the Santana Convent sherds (specially the 18th century ones). The multi-analytical characterization achieved in this study, points to the Dehua kilns as the most probable provenance for samples S11 and S12, of the Part [1] study.

Keywords: Chinese Porcelains; Santana convent; blue and white glazes; micro-Raman; XPS; GSDR; XRD; XRF; SM

1. Introduction

When, in 1498, Vasco da Gama arrived in Calicut (Kozhikode), on the Malabar Coast in the Indian Subcontinent, he was presented by the raja Samorim (Samuthiri) with thirteen Chinese porcelain vessels. The Portuguese captain would go on to acquire, at Chinese trading factory established there, a collection of porcelain to present his queen. From that time onwards, porcelain reached Europe via the maritime route that enable clear commercial, technique, and cultural interaction with the East.

Following the establishment of a permanent Portuguese trading post or factory in Macau in 1557, an intense maritime commercial network was developed between China and Portugal. Through this

 doi:10.20944/preprints202605.1370.v1

route, large quantities of porcelain, silk, spices, ivory, pearly, precious stones, and many other luxury goods reached Lisbon, from where many were redistributed throughout Europe. During the sixteenth and seventeenth centuries, Lisbon became one of the most important cosmopolitan commercial centres in Europe [2,3].

Several large Portuguese vessels belonging to the "Carreira das Índias" were wrecked along the African coastlines during this period. Chinese porcelain fragments recovered from these shipwrecks, collected off the South African or West African coasts, have provided valuable archaeometric information regarding export porcelains from the Ming and Qing dynasties [4,5]. However, most previous studies were based on relatively limited numbers of samples.

The catastrophic earthquake of 1755, which devastated much of Lisbon and its outskirts, also created exceptional archaeological contexts where many more sherds and sometimes almost complete vessels of Chinese porcelains could later be recovered from palaces, convents, monasteries, or in rich houses, domestic refuse deposits, wells, and garbage pits [6–10].

The Santana Convent in Lisbon, was constructed between 1561 and 1564, under the patronage of King John III and of his wife, Queen D. Catarina. It was a women´s religious house and remained operative until 1884, 50 years after the 1834 law, which abolished the religious orders and closed all convents and monasteries in Portugal.

Excavations directed by two of the co-authors (RVG and MVG) in the area it once occupied, that took place in 2002-2003 and 2009-2010, lead to the identification of many of its subterranean structures, as well as a vast assemblage of finds. Among these, around 1,800 pieces either complete or fragmentary corresponding to 500 Chinese vessels, were recovered in wells or garbage pits. They were mainly produced in the late 16th century and the following century and a few in the 18th century, used as tableware or for decorative purposes [7,9].

Porcelain richly painted in cobalt blue on white ground predominates and was produced in the kilns of Jingdezhen during the reigns of Jiajing and Wanli. Polychrome and gilded examples (kinrande and wucai) were also identified, as well as some bearing imperial symbolism and intended for the Chinese court.

In the present work, fifteen blue-and-white porcelain sherds of well-documented Chinese provenance were selected for comparative archaeometric characterization against the Lisbon fragments previously described in Part 1 [1].

a. The Fifteen Chinese Sherds Under Study

In Figure 1 we present all sherds under study in this work. S1 to S15 samples are porcelain sherds from well-known archaeologic Chinese provenance and dated from the 17th to 19th centuries. All dates indicated in the legend of Figure 1 are based in a stylistic evaluation.

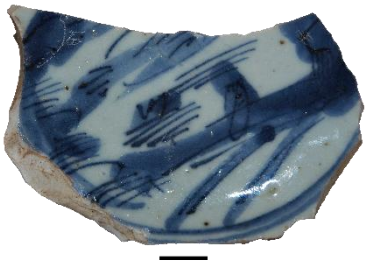

S1 – Jingdezhen kiln (Jingdezhen, Jiangxi),17th c. Bowl internal face.

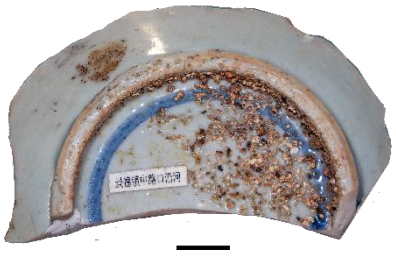

Bowl external face, with ring foot.

 doi:10.20944/preprints202605.1370.v1

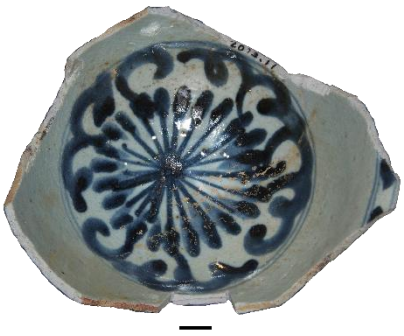

S2 – Jingdezhen kiln (Jingdezhen, Jiangxi),17th c. Bowl internal face.

Bowl external face, with ring foot.

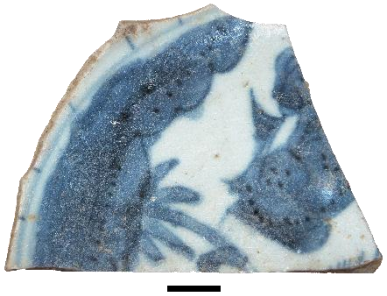

S3 – Anxi kiln (Quanzhou, Fujian): Zhuta Village kiln site. Late 17th c. Dish front face

Dish back face, with ring foot.

S4 – Anxi kiln (Quanzhou, Fujian): Zhuta Village kiln site, Late 17th c. Bowl internal face

Bowl external face.

S5 – Anxi kiln (Quanzhou, Fujian): Zhuta Village, Huoshaoban kiln site, Late 17th c. Bowl internal face

Bowl external face.

 doi:10.20944/preprints202605.1370.v1

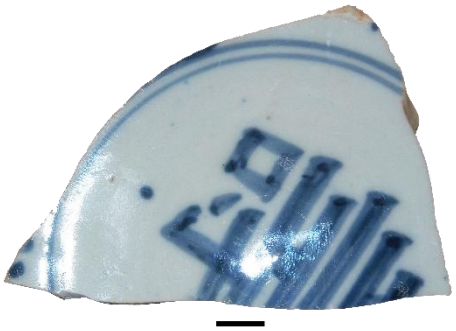

S6 – Dehua kiln (Quanzhou, Fujian): Neiban kiln site, Late 17th c. - 18thc. Dish front face

Dish back face, with ring foot.

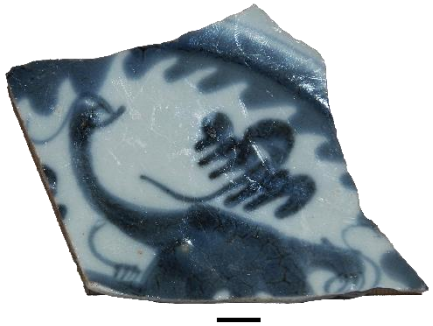

S7 – Dehua kiln (Quanzhou, Fujian): Dalongkou kiln site, 18thc. Dish front face

Dish back face, with ring foot.

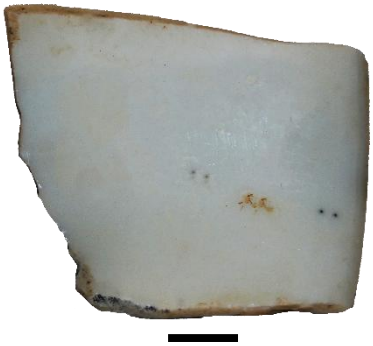

S8 – Dehua kiln (Quanzhou, Fujian): Dalongkou kiln site, 18thc. Bowl internal face.

Bowl external face

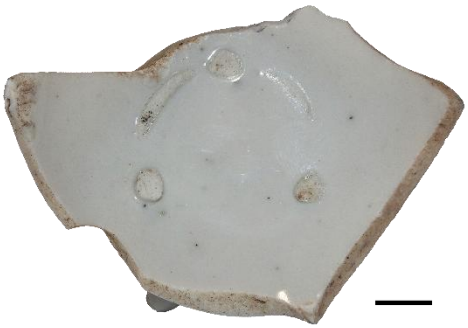

S9 – Dehua kiln (Quanzhou, Fujian): Dalongkou kiln site, 18thc. Bowl internal face.

Bowl external face, with ring foot.

 doi:10.20944/preprints202605.1370.v1

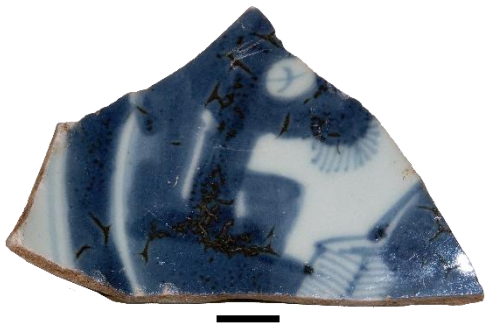

S10 – Dehua kiln (Quanzhou, Fujian): Dalongkou kiln site, 18thc. Bowl internal face.

Bowl external face, with ring foot.

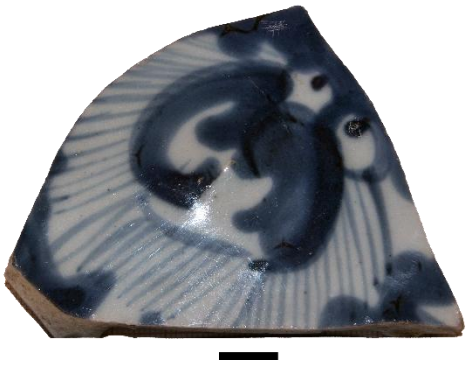

S11 – Dehua kiln (Quanzhou, Fujian): Dalongkou kiln site, 18thc. Dish front face

Dish back face, with remains of ring foot.

S12 – Dehua kiln (Quanzhou, Fujian): Dalongkou kiln site, 18thc. Bowl internal face.

Bowl external face, with ring foot.

 doi:10.20944/preprints202605.1370.v1

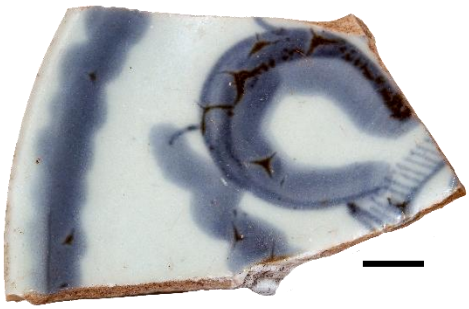

S13 – Dehua kiln (Quanzhou, Fujian): Dalongkou kiln site, 18thc. Bowl internal face

Bowl external face, with ring foot.

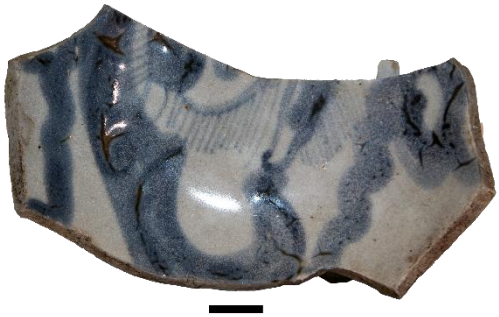

S14 – Dehua kiln (Quanzhou, Fujian): Dalongkou kiln site, 18thc. Bowl internal face

Bowl external face, with ring foot.

S15 Dehua kiln (Quanzhou, Fujian): Housno kiln site. Late 18thc. – 19th c. Bowl internal face

Bowl external face, with ring foot.

Figure 1. Samples S1 to S15 were porcelain sherds provided by the Chinese coworker of this manuscript (S L), allowing a comparison of those with the Lisbon sherds from the Santana Convent. These sherds are dated from the 17th to 19th centuries. All samples listed above are from the Chinese Qing Dynasty. Scale bar - 1 cm.

All samples studied here, in Part 2, are from the Qing Dynasty, and dated 17th and 18th century although sample S15 is dated late 18th century –19th century.

S1 and S2 are blue-and-white samples from the Jingdezhen kiln, province of Jiangxi, and are representative of the Jingdezhen production region in the 17th century.

Samples S3, S4, and S5 originate from the Anxi kilns. Anxi is a county within the Quanzhou region of Fujian Province. Its blue-and-white porcelain production is widely considered to have been strongly influenced by the Dehua kilns, while still exhibiting distinctive regional characteristics. Anxi

 doi:10.20944/preprints202605.1370.v1

production also formed part of the export-ware system and is often regarded as being of comparatively lower quality. At present, however, the differences between Anxi and Dehua production remain unclear with respect to body–glaze recipes and the sources or formulations of cobalt pigments.

The term "Dehua kilns" generally refers to the kiln-industry system located within the administrative boundaries of Dehua County, Fujian Province. To date, more than 200 kiln sites have been identified throughout the county. Among these, approximately 160 Qing-period kiln sites are recorded as having produced export porcelains, including both blue-and-white and white wares. These kiln sites are distributed across different townships and villages within the county, and in some villages more than ten kiln sites are concentrated within a single locality. Most kiln sites are identified by specific local place names. Consequently, the sherds described as "Dalongkou," "Neiban," and "Housno" refer to specific kiln-site localities within Dehua County. Although all belong to the broader "Dehua kiln system," they represent distinct production units situated in different locations across the county.

A large part of the blue-and-white fragments excavated from the Santana Convent were primarily attributed to Jingdezhen, 16th and 17th centuries. Many sherds studied in Part 1 were from the 17th century, Ming dynasty and some of them from the Wanli reign. Only samples S11 and S12 (from Part 1) were 18th century.

2. Experimental

GSDR experiments were conducted employing a home-built diffuse reflectance set-up, using an ICCD as detector and a W-Hal lamp as an excitation source. Three standards: Spectralon white disk, magnesium oxide and barium sulphate powder were used to obtain reflectance data. As a first step of this technique the reflectance R is determined as a function of the wavelength in the 250 to 750 nm range (UV, Vis and NIR spectral regions) and with the use of R and the Kubelka Munk equation the Remission Function (absorption spectra) are calculated.

X-ray Photoelectron Spectroscopy (XPS) was employed to investigate possible chemical differences between strongly pigmented dark-blue regions and weakly pigmented light-blue regions, particularly regarding cobalt and manganese. Two representative samples were analysed, S2 and S15, each of them in two different regions, one exhibiting intense dark-blue decoration and another showing light-blue pigmentation. Due to the shallow analytical depth of XPS (typically below 10 nm), superficial glaze layers were carefully scratched in selected areas to expose the pigment-rich regions. The scratched pieces were mounted onto the sample holder using double-sided conductive tape. Spectra were acquired using a Kratos XSAM800 dual-anode spectrometer operating with Al Kα radiation (hν = 1486.6 eV).

The power was set to 120 W. Samples were analysed in an ultrahigh-vacuum (UHV) chamber ($\approx 10^{-7}$ Pa) at room temperature, with an analysis angle of approximately 0° relative to the surface normal Spectra were collected with a 0.1 eV step size using Vision 2 for Windows software (Version 2.2.9, KRATOS). Data treatment and peak fitting were performed with XPSPeak 4.1 software using Shirley or linear background corrections and Gaussian–Lorentzian peak shapes.

No flood gun was used for neutralizing charge accumulation. Charging effects were corrected by setting the C 1s component of adventitious carbon to 285.0 eV [11,12]. Under these conditions, the Si 2p$_{3/2}$ peak remained constant at 103.0 eV in all the samples.

For quantification purposes, the sensitivity factors (SF) used were those furnished by the equipment library: 0.278 for C 1s, 0.78 for O 1s, 0.477 for N 1s, 2.393 for Co 2p$_{3/2}$, 0.328 for Si 2p, 0.193 for Al 2p and 2.659 for Mn 2p.

Micro-Raman spectroscopy proved to be particularly effective for identifying pigments, assessing glaze structure, and characterizing crystalline phases present in both glaze and ceramic body. Raman spectra were acquired directly on glazed surfaces using a confocal micro-Raman system under low laser power to avoid thermal alteration. The technique provided information regarding the silicate network organization of the glaze, as well as the occurrence of crystalline inclusions

 doi:10.20944/preprints202605.1370.v1

For elemental composition information, XRF analyses were performed using a Niton XL3T GOLDD spectrometer from Thermo Scientific.

To study the mineralogical and phase composition of the ceramic bodies and glazes of the porcelain sherds, XRD experiments of the powder crystalline phases were carried out by using of an X-ray diffractometer (Panalytical X´PERT PRO model), with CuKα radiation.

In the stereo microscopy (SM) experiments sherd features were observed using a Nikon SMZ645 stereomicroscope and representative images were acquired using a Moticam 10.0 MP digital camera.

Further details regarding all these techniques were previously described in [13–17].

3. Results

3.1. GSDR Spectra Glazes and Ceramic Bodies

From the reflectance curves (R) and using the Kubelka Munk function $F(R) = (1- R)^2/2R$, the UV–Vis-NIR absorption spectra of the sherds were obtained for all cases. The GSDR absorption spectra obtained for samples S2, S4, S6, S10, and S15 are representative of the entire group of studied porcelains and are presented in Figure 2.

GSDR spectra for sample S2, Jiangxi province, Jingdezhen kiln, 17th century.

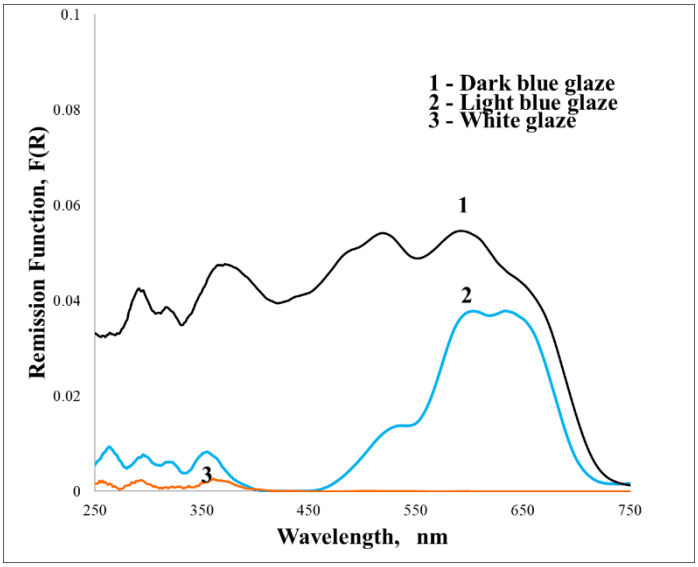

GSDR spectra for sample S4, Fujian province, Anxi, Zhuta kiln, late17th century.

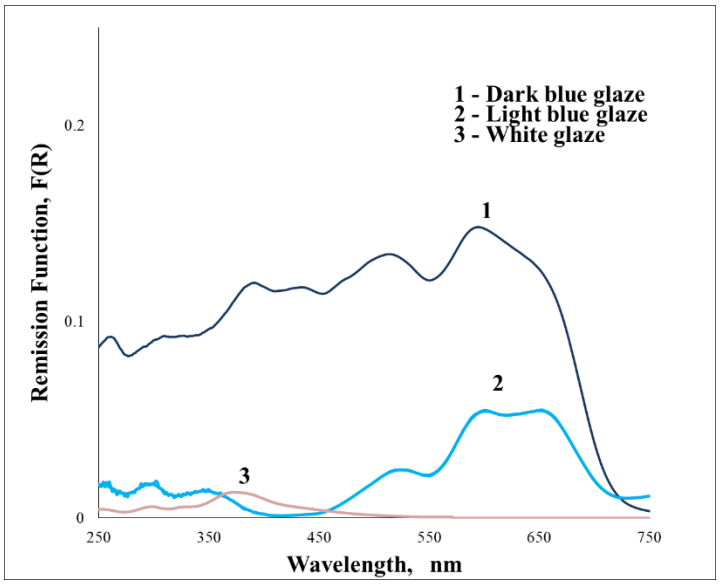

 doi:10.20944/preprints202605.1370.v1

GSDR spectra for sample S6, Fujian province, Dehua, Neiban kiln, late17th – early18th century.

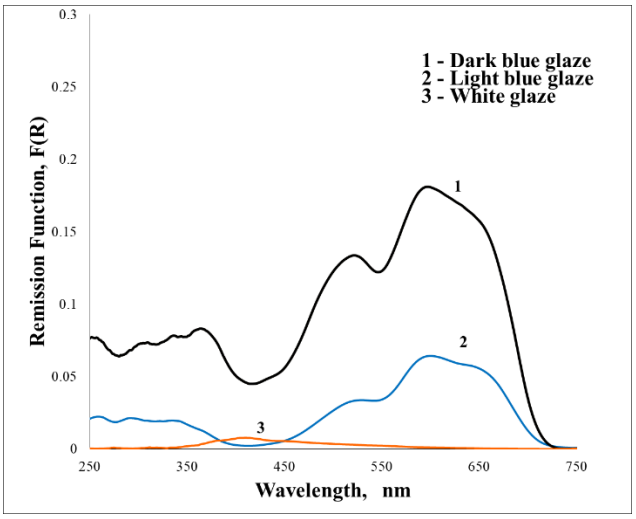

GSDR spectra for sample S10, Fujian province, Dehua, Dalongkou kiln, 18th century.

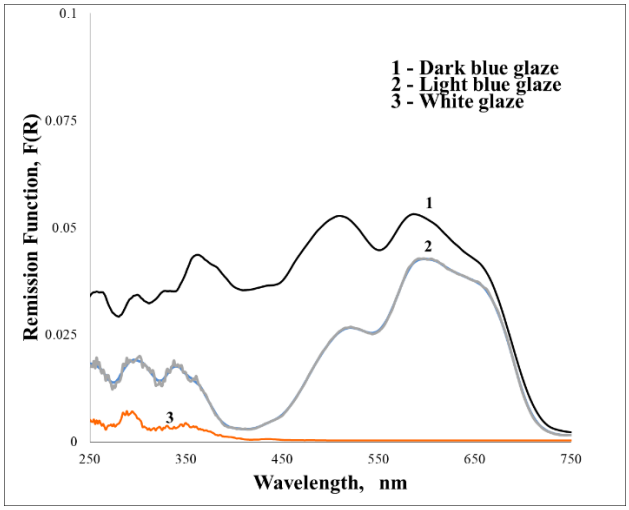

GSDR spectra for sample S15 Fujian province, Dehua, Housno kiln, late18th – early19th century.

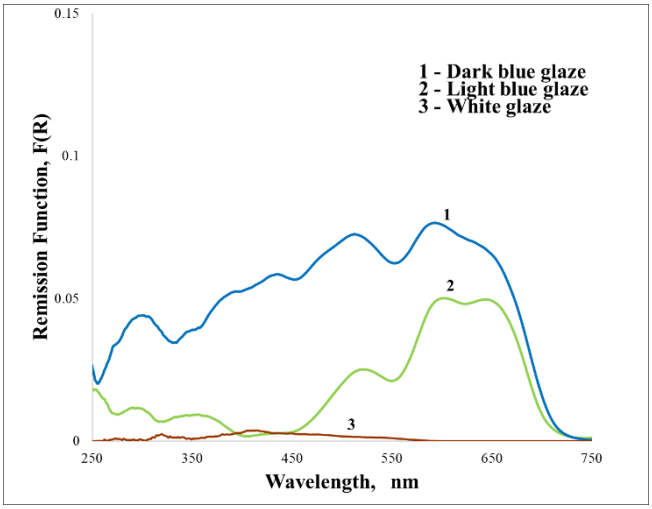

Figure 2. GSDR absorption spectra of Samples S2, S4, S6, S10 and S15, (1) Dark blue glaze, (2) Light blue glaze and (3) White glaze.

 doi:10.20944/preprints202605.1370.v1

Sample S2 GSDR absorption spectra are similar to those obtained for the sherd S1. The S4 GSDR absorption spectra are representative of the three Anxi kiln samples, while S10 spectra are like all Dehua, Dalongkou kiln ones. The GSDR spectra of S15, Dehua, Housno kiln are also quite similar to those of Dalongkou kilns. The exception is the S6 GSDR absorption spectra,

Clearly, in the porcelains S1 to S15 the dark blue and light blue pigments seem to be obtained with pigments of different cobalt origin, except for sample S6 where only one type of blue pigment seemed to have been applied, obviously in high or lower loadings.

The GSDR absorption spectra for the dark blue glaze of all samples presented in Figure 2 (except the S6 case) are similar to the one published for a 16th century Seville faience in a previous paper from our group [13], and to several dark blue glazes reported in [1]. When comparing with the light blue glaze, the reduced absorption in the 400-450 nm region, or even the 250-450 nm region exhibits now large absorptions, pointing to either a different cobalt species responsible for the absorption or even to a different pigment

The light blue glaze, for all the samples, exhibits three different absorption bands, located at about 524, 596 and 650 nm, which are characteristic of Co^{2+} in a tetrahedral environment. This is also the case for sample S6 in the dark blue glaze.

These absorption bands derive from spin and symmetry allowed electronic d-d transitions of Co^{2+} from the $^4A_2(F)$ ground state to the $^4T_1(P)$ excited state and from the $^4A_2(F)$ to the $^4T_1(F)$, and respective splittings [18,19]). Differences between the bands' relative intensities observed on different samples were ascribed to some variation in the glass matrix composition where the Co^{2+} ions are embedded [18–21].

For the Co^{2+} in an octahedral environment new bands appear on the ~250 to 450 nm region [18,21,22].

Figure 4 from Part 1 (reference [1]) presents the GSDR absorption spectra for sample S11 (similar data were observed for S12). S11 and S12 are 18th century productions. At this stage, these observations suggest the GSDR absorption spectra of dark blue, or to different oxidized forms of cobalt, Co^{2+} in different structural environments, or to different specific pigments of different origins.

The use of the X-Ray Photoelectron Spectroscopy as a surface analysis of the dark and light blue glazes provided us new information on these issues.

3.2. XPS Spectra for Dark Blue and Light Blue Glazes for Sample S15 and Sample S2

XPS, through the photoelectrons coming from the core, allows the detection and quantification of all the elements but He and H. A fine analysis of a specific photoelectron peak can also provide information about the oxidation state and/or about its atomic neighborhood, as well as, for transition elements, about the existence of unpaired electrons. However, as stated above, due to the extremely limited depth of analysis in XPS (less than 10 nm, depending on the photoelectron energy) an entirely non-destructive analysis of the pigment is impossible: the surficial glaze layer must be removed in order to have the pigment in the first surficial atomic layers. This operation was performed using a diamond pen. Two samples were submitted to this procedure: sample 2 and sample 15. For the latter one, the scratching yielded two dull surfaces keeping the colour difference existing before the scratching while for sample 2 the colour difference almost vanished.

Figure 3 displays the Co 2p and Mn 2p photoelectron regions for sample 15 in the dark and light blue zones. A typical Co 2p region presents a doublet, each component corresponding to a different spin-orbit coupling, characterized by a total angular momentum quantum number j=3/2 at a lower binding energy (BE), and j=1/2 at higher BE, the spin-orbit split being ~14.9 eV. For the ionic form Co^{2+}, the most intense component, Co $2p_{3/2}$, presents BE values in the literature ranging from 780.0 to 781.6 eV, when under the form of CoO. For the mixture of Co^{2+} and Co^{3+}, as in Co_3O_4, BE ranges from 779.3 and 780.7 eV [23,24]. In sample 15, both for the light and dark blue zones, a Co 2p typical spectrum could be obtained. The position of Co $2p_{3/2}$ component is different in the two zones studied as it is shown in Table 1.

 doi:10.20944/preprints202605.1370.v1

Spectra obtained for sample 2 in the binding energy range corresponding to Co 2p were impossible to treat adequately and, therefore, they will not be shown in the following.

For manganese, also the 2p region was chosen since it is the most intense. As a transition element, the Mn 2p region also presents two components, Mn $2p_{3/2}$, and Mn $2p_{1/2}$ with an intensity ratio around 2. The Mn $2p_{3/2}$ component is located at 641.9±0.1 eV whereas the component Mn $2p_{1/2}$ is at 653.7±0.1 eV. The position of the Mn $2p_{3/2}$ component and the spin-orbit split (11.8 eV), identifies the Mn as the Mn^{3+} species [24].

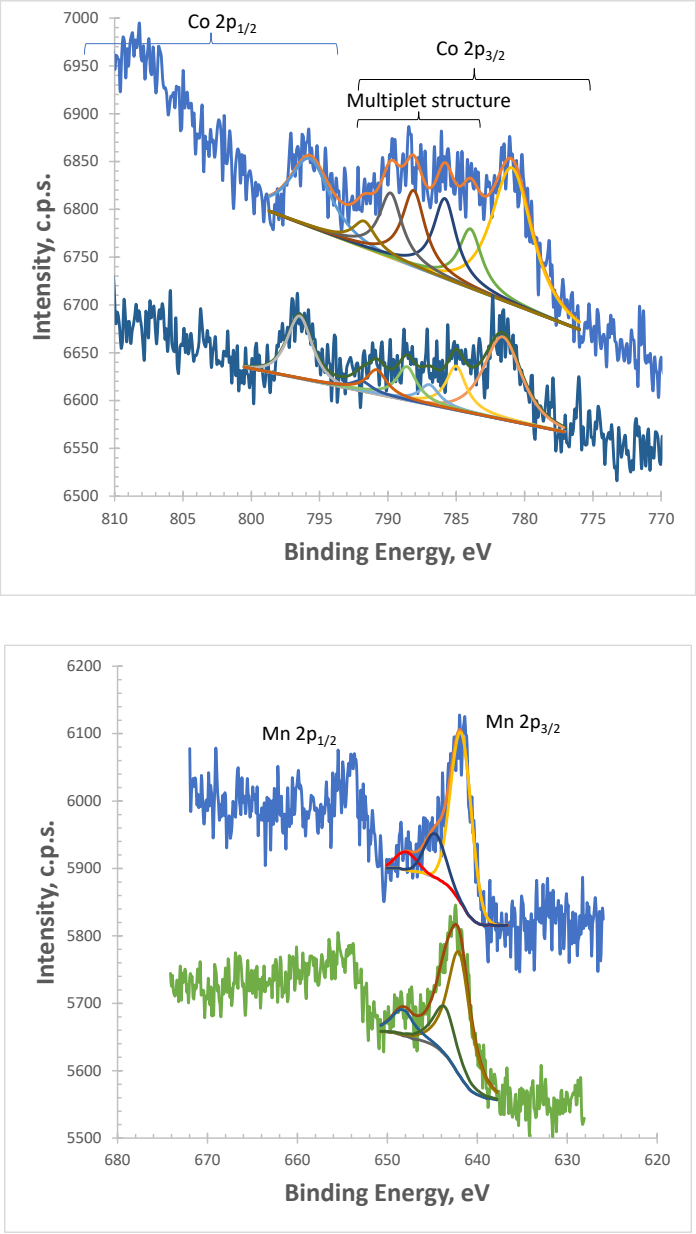

Figure 3. XPS Co 2p and Mn 2p spectra for samples 15. From bottom to top, light blue and dark blue.

Table 1 shows the details of BE and atomic % for the chosen elements:.

Table 1. XPS Binding energies, in eV, and atomic percentages for the main elements detected in sample 15 together with Co and Mn. Also the total atomic percentages and atomic ratios are presented at the end of the table.

	Dark blue		Light blue		Assignments
	BE	At.%	BE	At.%	

 doi:10.20944/preprints202605.1370.v1

C 1s 1	285.0	22.6	285.0	46.6	C-C, C-H sp^3 adventitious carbon
C 1s 2	286.7	5.7			C-O
C 1s 3	288.7	2.4	288.2	4.4	C=O
O 1s	532.3	51.9	532.4	37.2	
Al $2p_{3/2}$	74.5	1.7	74.8	1.4	Al^{3+}
Al $2p_{1/2}$	74.9	0.9	75.2	0.7	
Si $2p_{3/2}$	103.0	9.3	103.0	6.1	silica
Si $2p_{1/2}$	103.6	4.6	103.6	3.0	
Co $2p_{3/2}$	780.9	0.18	781.6	0.098	
Co multipl.	784.0	0.052	785.0	0.037	
Co multipl.	785.8	0.071	787.0	0.017	
Co multipl.	788.1	0.067	788.6	0.028	
Co multipl.	789.8	0.057	790.8	0.020	
Co multipl.	791.7	0.023	791.9	0.009	
Mn $2p_{3/2}$ 1	641.8	0.296	796.5	0.261	
Mn $2p_{3/2}$ 2	644.7	0.077	642.0	0.102	
Mn $2p_{3/2}$ 3	647.9	0.031	643.6	0.055	
Total Quantifications					
C		30.7		51.1	
O		51.9		37.2	
Al		2.6		2.1	
Si		13.9		9.1	
Co		0.45		0.21	
Mn		0.40		0.42	
Total Quantifications					
Si/Al		5.3		4.4	
Mn/Co		0.90		2.00	
$Co_{Multiplet}/Co_{total}$		0.60		0.53	
Co/Si		0.032		0.023	

The lower BE value of the C 1s region due to adventitious carbon, was taken as a reference to correct the charge accumulation in the sample and set to 285 eV. Oxygen O 1s region was fittable with a single, wide peak coming mainly from the aluminosilicate component of the sample. Al 2p an Si 2p were fit with single doublets as shown in Figure 3 and Table 1 and easily assignable to Al and Si in an aluminosilicate.

Mn 2p and, especially, Co 2p regions were acquired for a long time to improve the signal to noise ratio which, due to the very low relative amounts was rather poor.

Concerning the Co 2p region, the fitting region was extended to the end of the photoeleectron Co $2p_{1/2}$ peak to clearly show that the distance between the main features present corresponded well to the spin-orbit split expected in XPS Co 2p: 14.8±0.1 eV. However, since the fitting of the entire sub-region Co $2p_{1/2}$ (including also the multiplet structure) was difficult, just the Co $2p_{3/2}$ region components were used for quantitative purposes.

The striking difference observed between the two samples resides in the multiplet structure: in the dark zone, its relative importance is higher than in the light zone. Since the multiplet structure is due to the existence of unpaired electrons in the atomic species, this means that, at least in average, the Cobalt presents a higher spin in the dark blue zone than in the light blue zone. Another difference between the two samples is the average BE of the main Co $2p_{3/2}$ photoelectron peak which is lower in the dark zone (780.9 eV) than in the light zone (781.6 eV). The first difference is compatible with a larger fraction of high spin Co^{2+} ions in octahedral coordination than in the light zone where low spin Co^{2+} ions in tetrahedral coordination should prevail. The second difference may reinforce this statement since there are authors that argue that Co^{2+} in octahedral coordination presents a lower BE

 doi:10.20944/preprints202605.1370.v1

than the Co^{2+} in tetrahedral coordination [25]. Also, the difference, at least partly, may be due to the existence of some Co^{3+} in the dark zone, absent or less abundant in the light zone.

3.3. Micro Raman Spectra for Glazes and Ceramic Bodies

Raman micro-spectrometry can be used to obtain information regarding the crystalline or glassy structures [5], which are built from covalent bonds between the SiO_4 tetrahedra in different modes. The Raman parameters ratio of the bending (~500 cm^{-1}) and stretching (i.e. ~1000 cm^{-1}) envelopes, measured as the band area ratio Ip, the index of polymerization, proposed by Colomban [26–28], can be correlated to the glaze composition and processing temperature of the kiln.

 doi:10.20944/preprints202605.1370.v1

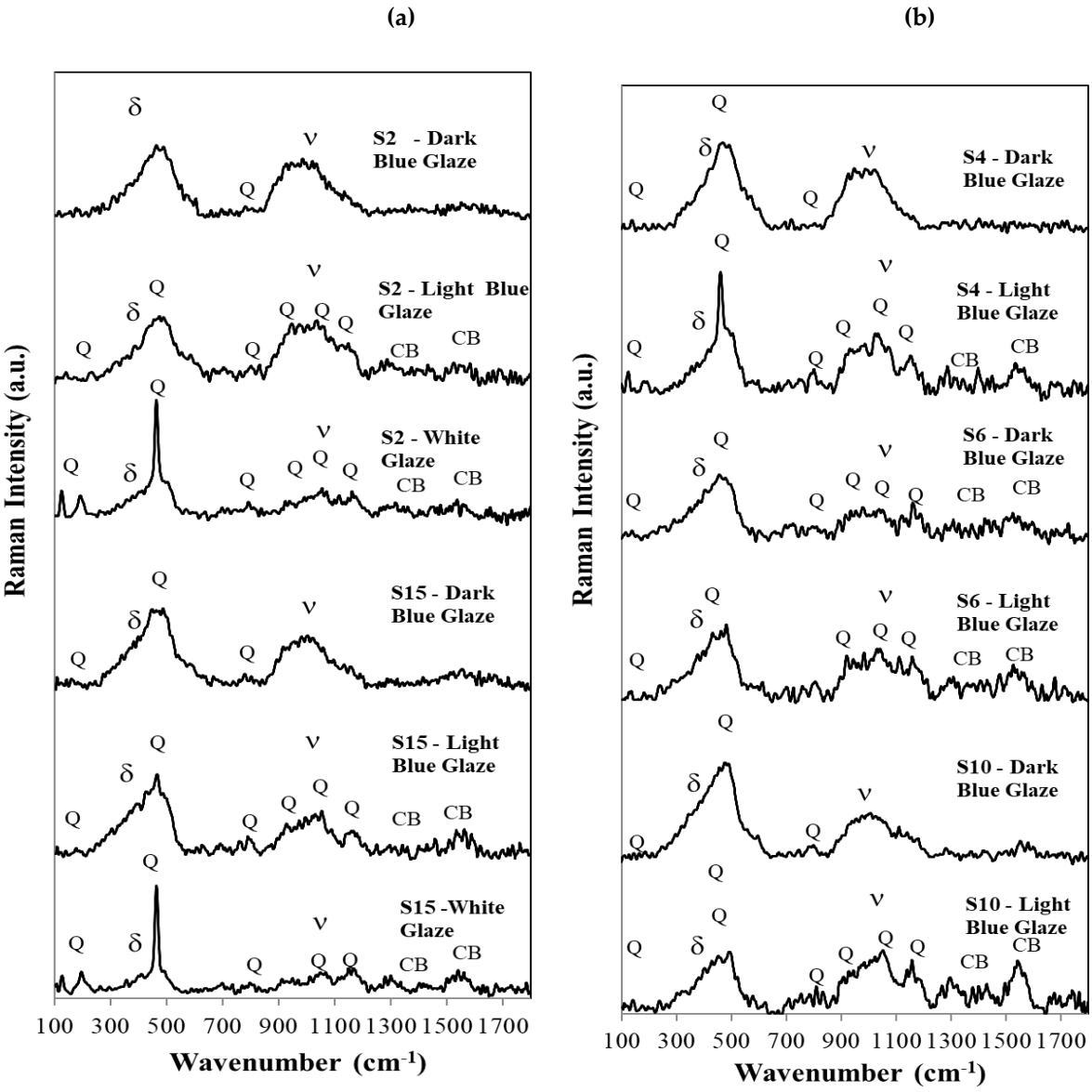

Figure 4. Micro-Raman glaze spectra: (a) S2 and S15 for the dark blue, light blue and white glazes; (b) S4, S6 and S10 for the dark blue glaze and light blue glazes. Q – Quartz, CB – Carbon Black, ◎ - stretching and ◎ – bending Raman envelopes of SiO_2.

The first observation is that in sample S2 (or S1) one cannot detect the Raman signatures of cobalt silicate Co_2SiO_4 or cobalt aluminate $CoAl_2O_4$ as the ones published in references [5,13,29]. The same happens in all the other samples, S3 to S15. This means the Co^{2+} concentration is low in all cases and the Co^{2+} ions are simply dissolved in the glaze matrix, without formation of crystalline cobalt silicate or aluminate phases, and showing no specific Raman signature as reported in other cases for Chinese porcelains [5].

In the dark blue spectra for samples S2, S4, S10 and S15, one can only observe the bending and the stretching bands of SiO_4, with maxima at about 483 and 1041 cm^{-1} respectively and, also, a small band at 793 cm^{-1} from the isolated tetrahedra (Q_0) [26,27]. For the light blue and white glazes, however, the Raman signature of crystalline quartz is superimposed on the bending and stretching envelopes of quartz, as Figure 4 consistently indicates. The light blue pigment is not so deep and strong as in the dark blue pigment and the crystalline quartz peaks becomes relevant.

In the case of the white glaze, the Raman spectrum is dominated by the crystalline signature of crystalline quartz, although mullite is also a strong presence, as we will show later in the corresponding diffraction patterns (powder XRD technique). In Figure 4a,b we do not label the small

 doi:10.20944/preprints202605.1370.v1

peaks at 505 nm (and very rarely the 513 nm peaks), but they exist and correspond to anorthite formations respectively, as again, the diffraction patterns will clearly show, later in the text.

Carbon black is also present in many Raman spectra of the 15 porcelain sherds under study here, but no calcium carbonate, gypsum or anatase could be detected in our samples.

3.4. Glaze and Body Microstructural Observations

Cross sections and interfaces of samples S1 to S15 were obtained with the use of a stereo microscopy device, providing some important information. Particular attention was paid to the distribution and size of cobalt-blue pigment particles, allowing for the distinction between under-glaze, in-glaze, and over-glaze decorative techniques [30].

Cross-sectional stereomicroscopy observations revealed important technological and microstructural features. Sherd thickness ranges from approximately 3–5 mm at vessel walls and rims to 7–10 mm at the base regions. The glaze layer generally varies between 200 and 300 μm in thickness.

In all analysed samples, cobalt pigment particles are dispersed within the superficial glaze layer, indicating predominantly in-glaze decorative techniques. No clear evidence of over-glaze decoration was identified.

Some samples, particularly S2, S11, and S14, exhibit pigment enrichment near the glaze–body interface, suggesting possible under-glaze application followed by glaze coating.

Several technological defects were also documented. Sample S1 exhibits large irregular pores, whereas sample S2 shows triangular shrinkage-related deformation structures. Samples S3 to S5 contain small rounded or irregular pores, while samples S6 to S15 commonly display elongated pores preferentially oriented parallel to the external surface.

These microstructural features likely reflect differences in paste preparation, firing atmosphere, firing temperature, and glaze viscosity during production.

 doi:10.20944/preprints202605.1370.v1

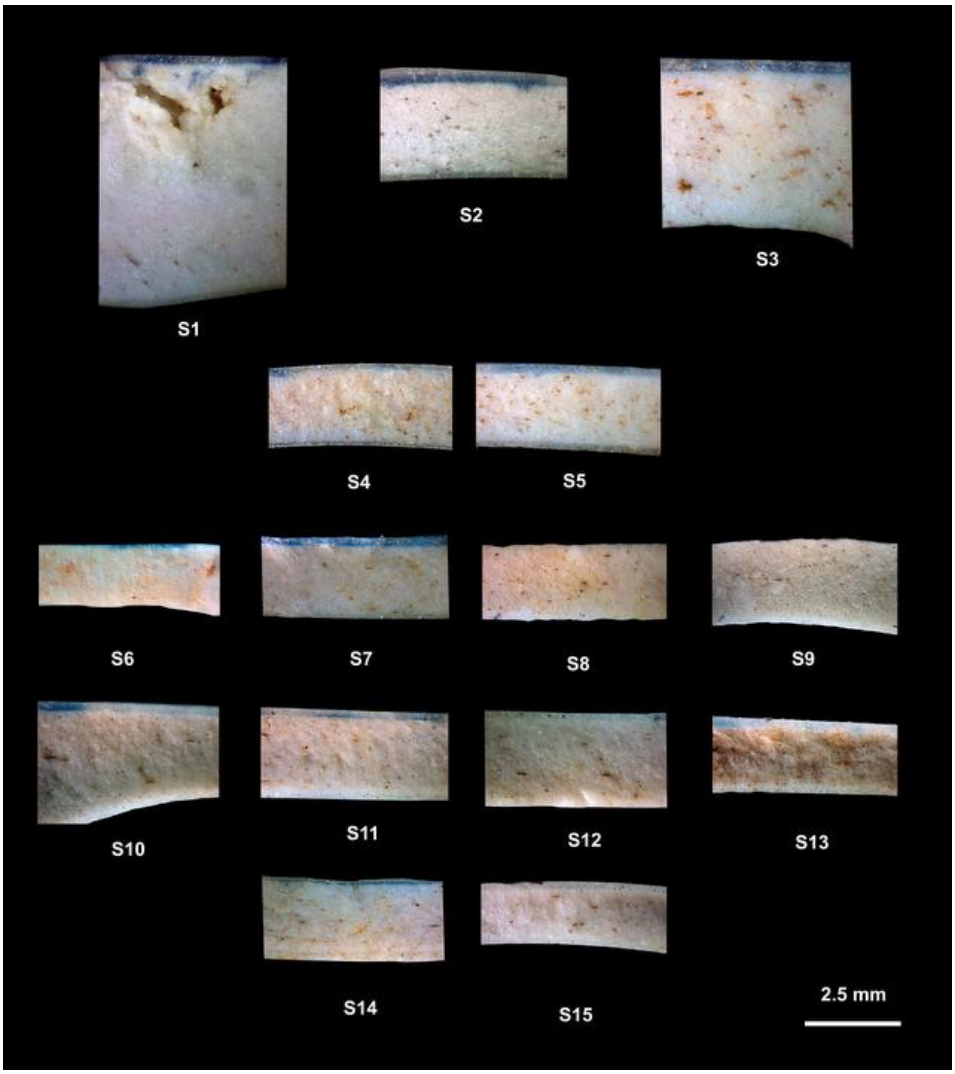

Figure 5. – Cross sections and interfaces of samples S1 to S15. Scale bar = 2.5 mm.

3.5. Star-Shaped Microfractures and Glaze Defects

Radiating star-shaped blue features are mainly identified in Dehua porcelains dated to the eighteenth century (S7, S10-S14), particularly those from the Dalongkou kiln site (Figure 6).

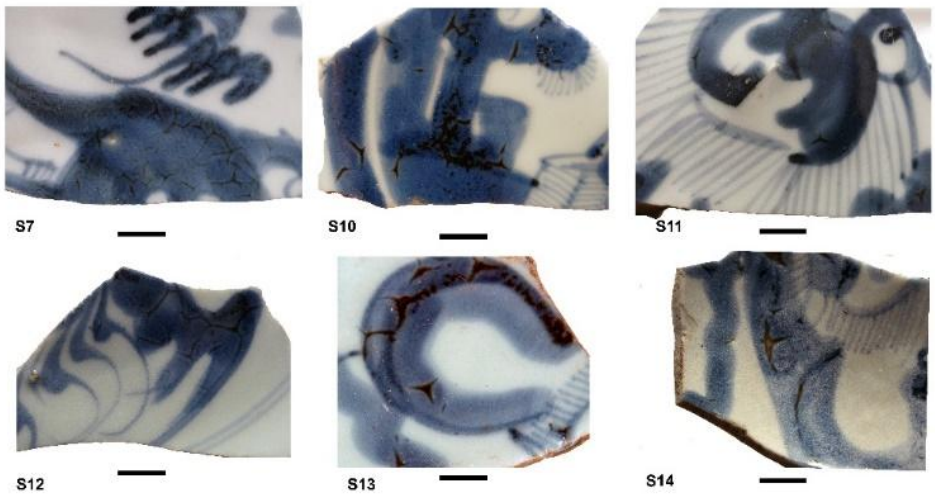

Figure 6. Star-shaped features in Dehua Dalongkou porcelains.

 doi:10.20944/preprints202605.1370.v1

Similar radiating blue features are also present in some Santana Convent samples, although generally less pronounced (Figure 7): S2 (subtle effect), sixteenth century; S6 (well defined effect), late seventeenth or early seventeenth century; S8 (subtle effect), late seventeenth century; S11 (strong effect), early eighteenth century; S12 (subtle effect), early eighteenth century.

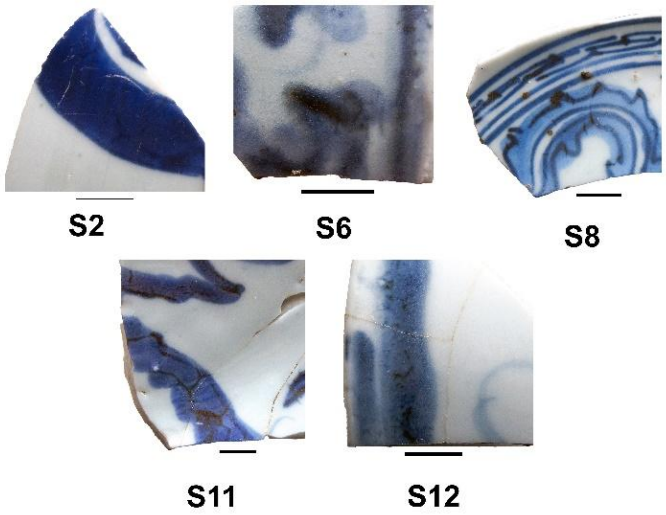

Figure 7. Star-shaped features in Santana Convent porcelains.

Sample S2 additionally presents star-shaped shrinkage structures developed within the ceramic body and amplified within both the white and blue glaze regions, frequently associated with a central cavity. Black spots containing large dendritic structures and crystalline aggregates were also observed at the center of the bowl.

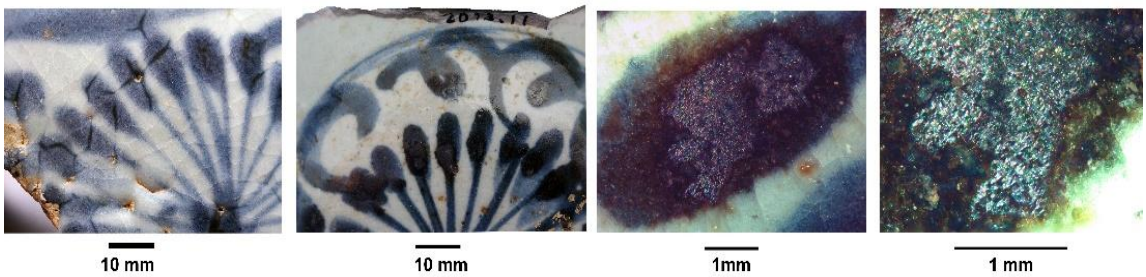

Figure 8. Star-shaped features and black spots inside dark blue glaze (S2 sample), presenting different colour halos and dendritic metallic inclusions.

3.6. XRD Data for Ceramic Bodies

Ceramic bodies and glazes from all the 15 samples listed in Figure 1 underwent comprehensive analysis using X-ray diffraction (XRD powder method), which provided information on the mineralogical and phase compositions of each sherd. Figure 9 shows a clear resemblance between diffractograms of all ceramic bodies.

In the evaluation of the diffractograms of Figure 9, one must pay attention to the fact that this technique uses powders (~10 to ~15 mg per essay). Due to the hardness of porcelain, it is very difficult to obtain the powder for each sample. So, ceramic bodies include some surficial glaze.

 doi:10.20944/preprints202605.1370.v1

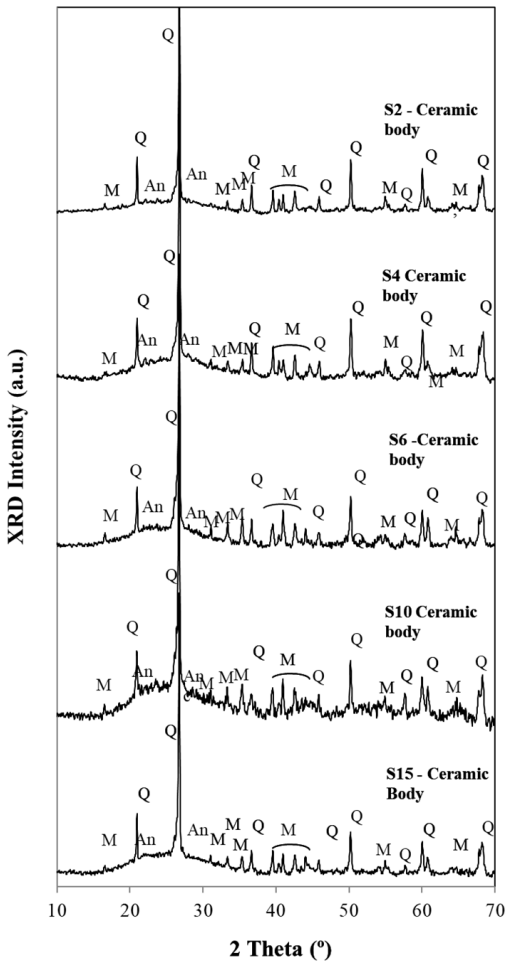

Figure 9. - Diffractograms for ceramic bodies of samples S2, S4, S6, S10 and S15. Q – Quartz (SiO_2), M – Mullite $(Al_2O_3)_3(SiO_2)_2$, An – Anorthite, $(CaO.\ Al_2O_3\ (SiO_2)_2$.

The phase composition of the fifteen ceramic bodies under study is relatively homogeneous. Quartz (SiO_2), mullite $(Al_2O_3)_3(SiO_2)_2$, and anorthite $(CaO.\ Al_2O_3\ (SiO_2)_2$ are the only crystalline phases identified in the diffractograms (Figure 9 and Table 1). Quartz is the dominant phase, with its characteristic diffraction peaks clearly visible in all samples. The persistence of quartz reflects the incomplete dissolution of silica grains during vitrification, a common feature of traditional hard-paste porcelains.

Mullite was identified in all ceramic bodies and constitutes an important mineralogical marker of high-temperature porcelain production. Its formation is associated with the transformation of alumina-rich clay minerals during firing and reflects both the elevated alumina content of the raw materials and the firing temperatures employed. According to the literature, firing temperatures of approximately 1250 °C are typical for porcelains with calcium-rich glazes, whereas temperatures close to 1350 °C are generally associated with porcelains containing calcium-poor glazes [5].

Anorthite occurs as a minor crystalline phase in most samples, indicating the presence of calcium-bearing components within the ceramic bodies and/or glaze formulations. Although less abundant than quartz and mullite, its recurrent presence suggests the systematic use of calcium fluxes during porcelain manufacture.

In the range between approximately 15° and 35° 2θ, all diffractograms exhibit a broad diffuse band assigned to an amorphous or nano-crystalline vitreous phase generated during high-temperature firing. The relative intensity of this vitreous contribution varies among the samples. Sample S10 presents the highest proportion of vitreous phase, indicating a greater degree of

 doi:10.20944/preprints202605.1370.v1

vitrification, whereas sample S2 displays the lowest vitreous contribution and a comparatively crystalline character. The remaining samples exhibit intermediate behaviour.

Overall, the coexistence of quartz, mullite, anorthite, and a significant vitreous phase is fully consistent with traditional Chinese hard-paste porcelain technology based on kaolin-rich raw materials and high-temperature kiln firing conditions.

Table 2. – XRD main peaks used to identify the minerals in the diffractograms for ceramic bodies and glazes.

Quartz - Q, SiO_2, 2θ◎◎= 21.0, 26.7, 36.7, 46.0, 50.2, 60.0, 64.1, 68.2
Mullite - M, $(Al_2O_3)_3(SiO_2)_2$, 2θ = 16.5, 26.4, 33.3, 35.4, 39.4, 40.8, 42.7, 49.6, 64.8
Anorthite – An, CaO. Al_2O_3 $(SiO_2)_2$, 2θ = 22.0, 27.5, 27.9, 30.3, 32.0, 38.0

3.7. XRF for the Dark Blue, Light Blue and White Glazes

XRF spectroscopy provided the elemental compositions of both white and blue glazes. The results obtained are in Table 3 and were obtained by irradiating the glazed surfaces of each sherd since this is a non-destructive technique

Table 3. Chemical composition of the dark blue, light blue and white glazes, obtained by XRF.

 doi:10.20944/preprints202605.1370.v1

Samples		MgO	Al₂O₃	SiO₂	K₂O	CaO	TiO₂	MnO	Fe₂O₃	CoO	NiO	CuO	ZnO	As₂O₃	Rb₂O	BaO	SnO₂	PbO
S1 17th c.	Dark blue glaze	nd/nq	8.34	73.66	2.80	12.24	0.05	1.49	1.11	0.15	0.06	0.01	0.01	0.01	0.01	0.03	nd/nq	nd/nq
	Light blue glaze	nd/nq	6.83	73.24	3.09	15.51	0.06	0.20	0.97	nd/nq	nd/nq	0.01	0.01	nd/nq	0.02	0.04	nd/nq	nd/nq
	White glaze	nd/nq	7.61	74.33	2.94	14.04	0.06	0.06	0.89	nd/nq	nd/nq	0.01	0.01	nd/nq	0.02	0.03	nd/nq	nd/nq
S2 17th c.	Dark blue glaze	nd/nq	9.49	72.01	3.15	11.34	0.07	1.69	1.82	0.30	0.05	0.01	0.01	nd/nq	0.01	0.02	nd/nq	nd/nq
	Light blue glaze	nd/nq	7.86	72.23	3.57	14.80	0.07	0.16	1.21	0.03	nd/nq	0.00	0.01	nd/nq	0.01	0.03	nd/nq	nd/nq
	White glaze	nd/nq	8.99	73.28	3.40	13.26	0.06	nd/nq	0.94	nd/nq	nd/nq	0.01	0.01	nd/nq	0.01	0.02	nd/nq	nd/nq
S3 Late 17th c.	Dark blue glaze	nd/nq	8.67	73.53	2.99	12.25	0.02	1.11	1.18	0.10	nd/nq	0.01	0.01	nd/nq	0.01	0.09	nd/nq	nd/nq
	Light blue glaze	nd/nq	8.34	74.89	3.15	12.14	0.03	0.49	0.81	0.04	nd/nq	0.01	0.01	nd/nq	0.01	0.06	nd/nq	nd/nq
	White glaze	nd/nq	8.73	74.75	3.49	12.33	0.04	nd/nq	0.58	nd/nq	nd/nq	nd/nq	0.01	nd/nq	0.01	0.03	nd/nq	nd/nq
S4 Late 17th c.	Dark blue glaze	nd/nq	9.60	70.02	2.52	12.56	nd/nq	3.45	1.30	0.41	0.03	0.01	nd/nq	nd/nq	0.01	0.05	nd/nq	nd/nq
	Light blue glaze	nd/nq	8.57	73.39	2.83	13.30	0.04	0.80	0.92	0.09	nd/nq	nd/nq	nd/nq	nd/nq	0.01	0.02	nd/nq	nd/nq
	White glaze	1.01	8.52	72.59	2.88	14.15	0.03	nd/nq	0.78	nd/nq	nd/nq	nd/nq	nd/nq	nd/nq	nd/nq	nd/nq	nd/nq	nd/nq
S5 Late 17th c.	Dark blue glaze	1.01	11.05	72.00	2.65	8.98	nd/nq	2.85	1.06	0.33	0.01	nd/nq	nd/nq	nd/nq	0.01	0.04	nd/nq	nd/nq
	Light blue glaze	nd/nq	11.45	73.42	2.72	10.86	0.03	0.65	0.95	0.07	nd/nq	nd/nq	nd/nq	nd/nq	0.01	0.01	nd/nq	nd/nq
	White glaze	nd/nq	10.77	74.38	2.79	11.07	0.03	0.06	0.86	nd/nq	nd/nq	nd/nq	nd/nq	nd/nq	0.01	0.01	nd/nq	nd/nq
S6 Late 17th- 18th c.	Dark blue glaze	nd/nq	7.74	75.40	4.78	9.26	0.06	1.66	0.73	0.29	nd/nq	0.01	0.01	nd/nq	0.01	0.02	nd/nq	0.01
	Light blue glaze	nd/nq	8.80	76.18	4.35	7.93	0.04	0.88	0.65	0.13	nd/nq	nd/nq	0.01	nd/nq	0.01	0.02	nd/nq	0.01
	White glaze	nd/nq	7.65	76.92	5.06	9.54	0.05	0.09	0.64	nd/nq	nd/nq	0.01	0.01	nd/nq	0.01	0.02	nd/nq	nd/nq
S7 18th c.	Dark blue glaze	nd/nq	8.21	71.53	6.44	6.59	nd/nq	5.63	0.96	0.41	nd/nq	0.02	0.02	nd/nq	0.01	0.11	nd/nq	0.04
	Light blue glaze	nd/nq	8.45	73.92	6.47	6.68	0.06	3.13	0.87	0.23	nd/nq	0.01	0.01	nd/nq	0.01	0.08	nd/nq	0.04
	White glaze	0.00	7.96	75.76	6.40	8.81	0.07	0.11	0.71	nd/nq	nd/nq	0.01	0.01	nd/nq	0.01	0.09	nd/nq	nd/nq
S8 18th c.	White glaze	nd/nq	8.04	78.09	6.82	6.33	0.05	0.09	0.45	nd/nq	nd/nq	nd/nq	nd/nq	nd/nq	0.01	0.07	nd/nq	0.01
S9 18th c.	White glaze	1.48	5.98	77.88	7.05	6.66	0.04	0.37	0.42	nd/nq	nd/nq	nd/nq	nd/nq	nd/nq	0.02	0.05	nd/nq	0.01
S10 18th c.	Dark blue glaze	nd/nq	6.77	73.04	5.70	7.51	nd/nq	4.43	1.72	0.39	0.14	0.04	0.01	nd/nq	0.01	0.14	nd/nq	0.05
	Light blue glaze	nd/nq	5.66	77.55	6.31	8.45	0.07	0.53	1.08	0.07	0.05	0.03	0.01	nd/nq	0.01	0.07	nd/nq	0.05
	White glaze	nd/nq	7.94	79.25	5.20	6.61	0.06	0.05	0.79	nd/nq	nd/nq	0.02	0.01	nd/nq	0.01	0.05	nd/nq	nd/nq
S11 18th c.	Dark blue glaze	nd/nq	7.60	72.89	4.34	12.12	0.05	1.66	0.95	0.15	0.05	0.03	0.01	nd/nq	0.01	0.11	nd/nq	0.01
	Light blue glaze	nd/nq	7.87	74.56	4.45	11.25	0.04	0.82	0.76	0.06	0.01	0.03	0.01	nd/nq	0.01	0.09	nd/nq	0.01
	White glaze	nd/nq	8.34	74.45	4.83	11.32	0.06	0.13	0.76	nd/nq	nd/nq	0.02	0.01	nd/nq	0.01	0.05	nd/nq	nd/nq
S12 18th c.	Dark blue glaze	nd/nq	9.05	70.19	5.63	9.38	0.05	4.04	0.97	0.36	0.06	0.03	0.01	nd/nq	0.01	0.14	nd/nq	0.02
	Light blue glaze	nd/nq	9.61	72.87	5.58	9.90	0.06	0.93	0.77	0.08	0.02	0.02	0.01	nd/nq	0.01	0.09	nd/nq	0.02
	White glaze	nd/nq	8.51	73.30	6.03	11.29	0.08	nd/nq	0.65	nd/nq	nd/nq	0.02	0.01	nd/nq	0.01	0.06	nd/nq	nd/nq
S13 18th c.	Dark blue glaze	nd/nq	6.70	75.91	4.61	8.84	nd/nq	2.31	1.26	0.19	nd/nq	nd/nq	nd/nq	nd/nq	0.01	0.02	0.02	0.00
	Light blue glaze	nd/nq	8.13	78.87	4.28	7.46	0.07	0.26	0.80	nd/nq	nd/nq	0.01	0.01	nd/nq	0.01	0.11	nd/nq	0.01
	White glaze	nd/nq	7.94	78.61	4.56	7.98	0.06	0.04	0.73	nd/nq	nd/nq	0.01	0.01	nd/nq	0.01	0.02	nd/nq	0.00
S14 18th c.	Dark blue glaze	nd/nq	4.81	74.89	5.61	11.88	0.07	1.50	0.91	0.09	nd/nq	nd/nq	0.01	nd/nq	0.01	0.17	nd/nq	0.01
	Light blue glaze	nd/nq	8.37	77.10	4.27	9.50	0.05	0.11	0.48	nd/nq	nd/nq	0.01	0.01	nd/nq	0.01	0.07	nd/nq	0.01
	White glaze	nd/nq	7.40	77.83	4.62	9.53	0.05	0.00	0.46	nd/nq	nd/nq	0.01	0.01	nd/nq	0.01	0.05	nd/nq	nd/nq
S15 Late 18th c.- Early 19th	Dark blue glaze	1.40	8.28	71.87	3.95	7.46	nd/nq	5.55	0.96	0.32	0.03	0.01	0.01	nd/nq	0.01	0.09	nd/nq	0.01
	Light blue glaze	nd/nq	8.52	73.16	3.90	7.62	nd/nq	5.38	0.94	0.30	0.02	0.01	0.01	nd/nq	0.01	0.09	nd/nq	0.01
	White glaze	nd/nq	7.95	77.65	4.36	9.19	0.07	0.09	nd/nq	nd/nq	nd/nq	0.01	0.01	nd/nq	0.01	0.04	nd/nq	nd/nq

A global analysis of the results shows that, in general, the glazes with a bluish color are slightly less siliceous and calcic, and, as would be expected, are more cobaltic, to which Fe and Ni are added. The white pastes do not contain Co and Ni and have very little Mn, which reveals that the pigment, in addition to Co, is enriched in Mn and Fe.

In the Dehua samples, the average values of Al_2O_3 and CaO, both in the coloured and white glazes, are lower than the average of the full set of samples, respectively 8.22% and 4.4%. Conversely, the values of K_2O, MnO, FeO, CoO and NiO are higher than the average of the set. Trace elements such as Cu, Zn, Pb, and Sn are present in very low concentrations or below detection limits.

4. Discussion

The GSDR results show systematic differences between dark and light blue glazes,-In the latter ones, the presence of three well-defined absorption bands at approximately 524, 596, and 650 nm in light blue regions is characteristic of Co^{2+} ions in tetrahedral coordination. In contrast, dark blue glazes exhibit further absorption features previously described, suggesting differences in cobalt coordination environment. These differences are consistent across most samples and can be explained by pigment concentration or by the use of different pigments. The spectra obtained for Dehua, Jingdezhen, and Anxi productions suggest the use of pigment application technologies or even distinct cobalt sources [18–22].

 doi:10.20944/preprints202605.1370.v1

The XPS results reinforce the interpretation derived from the GSDR data. In sample S15, the Co $2p_{3/2}$ binding energy is lower in the dark blue region (780.9 eV) than in the light blue region (781.6 eV), and the multiplet structure is more pronounced in the darker glaze. These observations are compatible with a greater contribution of high-spin cobalt species and consequent differences in cobalt coordination geometry between dark and light blue regions [24,25]. Furthermore, the higher Mn/Co ratio observed in the light blue glaze, together with the higher cobalt concentration in dark blue regions, may suggest that different pigments were employed during glaze preparation.

Micro-Raman spectroscopy confirms that cobalt is not present as a crystalline phase but rather as dissolved Co^{2+} ions within the amorphous silicate glaze matrix. No Raman signatures corresponding to cobalt silicate or cobalt aluminate crystalline phases were detected in any of the analysed samples, indicating efficient incorporation of cobalt into the vitreous network during high-temperature firing [26–30]. The Raman spectra are dominated by the characteristic silicate bending and stretching envelopes around ~500 and ~1000 cm^{-1}, consistent with highly vitrified glazes. In the light blue and white glazes, the increased visibility of quartz Raman peaks reflects lower pigment concentrations and greater optical transparency. The absence of crystalline cobalt compounds is fully compatible with previous studies of Chinese blue-and-white porcelains, where cobalt generally behaves as a network modifier dissolved in the glaze structure [26–30].

The microstructural observations obtained by stereomicroscopy reveal important technological differences between the studied porcelains. Several glaze and body defects were identified, including rounded and elongated pores, shrinkage-related cavities, pigment accumulations, and irregular deformation structures. These features reflect variations in paste preparation, glaze viscosity, firing atmosphere, firing temperature, and cooling dynamics. In some samples, particularly S2, S11, and S14, cobalt enrichment near the glaze–body interface suggests underglaze application followed by glaze coating and partial cobalt migration during firing.

The XRD analyses indicate a relatively homogeneous mineralogical composition among all the studied porcelain bodies. Quartz and mullite are the dominant crystalline phases, while anorthite appears as a minor component. Mullite formation confirms firing temperatures characteristic of traditional Chinese hard-paste porcelain technology, typically above 1250 °C [31]. The recurrent presence of anorthite suggests the use of calcium-rich components or fluxes in ceramic formulations.

The XRF analyses complement these observations by showing that blue glazes are systematically enriched in Co, Mn, Fe, and Ni, whereas white glazes contain only residual amounts of these elements. Dehua samples exhibit relatively higher concentrations of transition metals when compared with Jingdezhen and Anxi productions, suggesting distinct raw material procurement strategies and pigment preparation methods within the regional kiln systems. These compositional differences reinforce the evidence for technological variability among Chinese export porcelain production centers.

The transition-metal impurity signatures identified by XRF and some by XPS provide important archaeometric information regarding cobalt provenance. In historical blue-and-white porcelains, Persian cobalt sources are typically characterized by elevated arsenic and nickel contents combined with relatively low manganese concentrations, whereas Chinese domestic cobalt ores commonly exhibit low arsenic and comparatively higher Mn/Co and Fe/Co ratios [32,33]. The very low arsenic contents observed in the present samples (<0.05 wt.% As_2O_3), together with the relatively elevated manganese concentrations and Mn/Co ratios, strongly suggest the predominance of domestic Chinese cobalt sources rather than imported Persian cobalt. These observations are fully compatible with Qing-period cobalt exploitation and pigment preparation technologies associated with Fujian and Dehua kiln systems. The compositional variability observed between dark and light blue regions further suggests the use of heterogeneous cobalt-bearing raw materials and/or different pigment-processing strategies during glaze preparation.

Particularly significant are the radiating triangular or star-shaped features identified predominantly in the Dehua porcelains, especially those associated with the Dalongkou kiln site. These structures represent a previously underreported class of glaze defects in Chinese export

 doi:10.20944/preprints202605.1370.v1

porcelains. Rather than corresponding to intentional decorative motifs, they are interpreted as the result of localized physicochemical processes occurring during glaze melting, vitrification, and cooling. Their morphology and spatial distribution strongly suggest an association with microstructural heterogeneities and stress development within the glaze layer.

Microscopic observations demonstrate that these features are systematically associated with gas bubbles, cavities, dendritic inclusions, and localized crystalline aggregates within the glaze. Such heterogeneities are widely recognized as products of incomplete degassing during firing, particularly in viscous silicate melts [34,35]. During cooling, these discontinuities act as stress concentrators, promoting the nucleation and propagation of microfractures. The observed radiating and frequently triangular geometries are fully consistent with fracture propagation mechanisms described for brittle glassy materials subjected to constrained thermal conditions [36].

In sample S2, the occurrence of shrinkage-related star-shaped structures extending from the ceramic body into the glaze suggests that at least part of the defect formation originated during paste contraction and was subsequently amplified during glaze cooling. The frequent presence of a central cavity supports the interpretation that trapped gases or localized heterogeneities acted as nucleation centers for fracture propagation. The associated black spots containing dendritic metallic structures and white crystalline aggregates further indicate complex interactions between impurity segregation, localized crystallization, and glaze evolution.

From a technological perspective, the formation of these glaze defects is fully compatible with the production context of the Dehua kiln system during the Qing dynasty. Historical and archaeometric studies emphasize the decentralized nature of porcelain manufacture in Fujian province, involving numerous kiln sites operating with variable control over raw materials, glaze recipes, firing temperatures, kiln atmospheres, and cooling rates [31,37,38]. Such variability directly affects critical parameters including glaze viscosity, gas release, thermal expansion mismatch between glaze and body, and cooling dynamics, all of which strongly influence defect formation and glaze stability.

Previous archaeometric investigations of Chinese export porcelains have documented the frequent occurrence of glaze heterogeneities, including bubbles, inclusions, and compositional fluctuations, particularly in productions associated with less controlled firing conditions [31]. Although glaze heterogeneities and cooling-related microfractures are well documented in historical porcelains, the systematic association of radiating cobalt-enriched star-shaped features with Dehua export wares appears to have received limited attention in archaeometric literature.

Importantly, the presence of similar features in selected Santana Convent porcelains, particularly in samples S11 and S12, together with the spectroscopic, compositional, and mineralogical similarities identified in this study, strengthens the attribution of these Lisbon fragments to Dehua kiln production. These observations also reinforce the evidence for the circulation of Dehua export porcelains through the maritime trade networks connecting Fujian, Macau, Lisbon, and broader European markets during the seventeenth and eighteenth centuries [2–10].

From a broader heritage and archaeometric perspective, these results demonstrate that glaze defects and microstructural imperfections, often regarded merely as secondary technological artefacts, can provide highly relevant information for provenance studies. When integrated with spectroscopic, compositional, mineralogical, and microstructural analyses, these features significantly strengthen the archaeometric characterization of eighteenth-century Chinese export porcelains and contribute to a better understanding of technological variability associated with intensified export-oriented production during the Qing dynasty.

Taken together, the analytical data consistently indicate that technological variability among the studied porcelains reflects differences in cobalt sources, glaze preparation, firing conditions, and kiln practices across the Jingdezhen, Anxi, and Dehua production systems. In particular, the recurrent occurrence of star-shaped cobalt-enriched microfractures in Dehua porcelains, combined with the spectroscopic and compositional similarities observed in selected Santana Convent samples, provides

 doi:10.20944/preprints202605.1370.v1

strong support for attributing part of the Lisbon assemblage to Dehua production. These observations establish the basis for the broader provenance interpretations and technological implications discussed in the Conclusions section, while reinforcing the value of combining complementary analytical techniques for the study of Chinese export porcelains and their circulation through early modern maritime trade networks.

5. Conclusions

The results obtained in this study demonstrate that the integration of spectroscopic, compositional, mineralogical, and microstructural analyses provides a robust framework for the characterization and provenance assessment of Chinese blue-and-white porcelains, particularly within the context of archaeological assemblages from Santana Convent.

GSDR, XRF and XPS analyses reveal systematic differences between dark and light blue glazes, reflecting variations in cobalt coordination environment and chemical composition rather than simple concentration effects. These results indicate different cobalt in glaze environments or the use of distinct preparation methods or even pigments., consistent with the coexistence of multiple technological traditions associated with major Chinese production centres such as Jingdezhen and Dehua.

Raman spectroscopy confirms that cobalt is predominantly present as Co^{2+} ions dissolved in the amorphous glaze matrix, while XRD results show a consistent mineralogical composition dominated by quartz and mullite, indicative of high firing temperatures typical of Chinese hard-paste porcelain. The presence of anorthite further reflects the use of calcium-based fluxes. XRF data highlight compositional differences between glaze types and show that Dehua samples are characterized by relatively higher concentrations of transition metals (Co, Mn, Fe, Ni), suggesting distinct raw material selection and technological practices within regional kiln systems. The very low arsenic contents (<0.05 wt.% As_2O_3), combined with relatively high manganese concentrations and Mn/Co ratios, indicate that the cobalt used in the present samples was predominantly derived from domestic Chinese sources rather than imported Persian cobalt.

Microstructural analyses demonstrate that glaze defects provide valuable technological information. In particular, the identification of radiating star-shaped microfractures constitutes a significant finding. These features are interpreted as cooling-induced defects associated with gas entrapment, stress development, and cobalt redistribution within the glaze. Their occurrence is systematic in Dehua porcelains, especially those attributed to the Dalongkou kiln site. The presence of similar features in some of the Santana Convent samples, combined with spectroscopic and compositional data, strengthens the attribution of selected fragments to Dehua kiln production and reflects the circulation of these wares through early modern trade networks linking China and Lisbon, particularly within the context of Portuguese maritime expansion and consumption patterns.

From a broader heritage perspective, this study highlights the importance of integrating multiple analytical approaches to improve the reliability of provenance assessment and to better understand technological variability in Chinese porcelain production. To our knowledge, XPS is not usually employed in archaeometric studies of the type reported here. However, its application to one of the samples (S15) proved to be a highly promising complementary technique to the more conventional methods. In particular, it enabled the assignment of the spectral features observed in the dark blue regions (GSRD spectra) within the 250–450 nm range to high-spin Co^{2+} species in octahedral coordination, rather than to a different pigment component (e.g., manganese-based species). This conclusion was made possible by the ability of XPS to distinguish between high- and low-spin states of transition metals. The surface sensitivity of XPS can be mitigated through the use of synchrotron-based XPS facilities, where the photoelectron escape depth can be significantly increased by employing higher-energy incident X-radiation. This approach avoids the need to scratch the glaze layer, thereby reducing the risk of removing part of the pigment together with the glaze.

The analyses, whose results are now presented, suggest that, during the late sixteenth and seventeenth centuries, the Portuguese obtained their supplies chiefly from Jingdezhen. However,

 doi:10.20944/preprints202605.1370.v1

over the following two centuries, owing not only to Portuguese demand but also to that of the English and the Dutch, through their powerful trading companies established in the East, the consumption of porcelain appears to have risen exponentially, and production centres such as Quanzhou, in Fujian Province, either emerged or underwent significant development.

Acknowledgments: This work is financed by national funds from FCT - Fundação para a Ciência e a Tecnologia, I.P., in the scope of the project UIDB/04565/2020 and UIDP/04565/2020 of the Research Unit Institute for Bioengineering and Biosciences – iBB.

References

1. Vieira Ferreira, L.F.; Machado, I.F.; Varela Gomes, R.; Varela Gomes, M.; Pereira, M.F.C. An Archaeometric Study of Twelve Porcelain Chinese Sherds Found at the Santana Convent in Lisbon—16th to 18th Centuries. *Heritage* **2025**, *8*, 253-273. https://doi.org/10.3390/heritage8070253
2. Casimiro, T.M. Globalization, trade, and material culture: Portugal's role in the making of a multicultural Europe (1415–1806). *Post-Medieval Archaeology* **2020**, *54*, 1-17. https://doi.org/10.108000794236.2020.1750239
3. Varela Gomes, M.; Casimiro, T.M.(Eds.) *On the World´s Routes. Portuguese Faience (16th -18th centuries)*. Instituto de Arqueologia e Paleociências, Universidade Nova de Lisboa. Lisboa, 2013.
4. de Waals, D. Raman investigation of the ceramics from the 16th and 17th century Portuguese shipwrecks. *J. Raman Spectrosc.* **2004**, *35*, 646–649. https://doi.org/10.1002/jrs.1210
5. Colomban, Ph.; Ngo, A.; Edwards, H.G.M.; Prinsloo, L.C.; Esterhuizen. L.V. Raman identification of the different glazing technologies of Blue-and-White Ming porcelains, *Ceram. Int.* **2022**, *48*, 1673–1681. https://doi.org/10.1016/j.ceramint.2021.09.246
6. Varela Gomes, M.; Varela Gomes, R.; Casimiro, T.M. Convents, monasteries and porcelain: a case study of Santana Convent, Lisbon, Global Pottery 1, Historical Archaeology and Archaeometry for Societies in Contact, *British Archaeological Reports, I.S.* **2015**, *2761*, 93-101.
7. Xiong, H.; Varela Gomes, M.; Varela Gomes, R.; Gonçalves, J.; Li, S. Chinese Porcelain Marks Found at the Santana Convent in Lisbon, *Europa Post Mediavalis* **2022**, *3*, 115–127.
8. Shanshan, L.; Varela Gomes, M.; Varela Gomes, R.; Xiong, H. Discovering kinrande porcelain excavated in Portugal, Post-Medieval Archaeology **2025**, 300-322, https://doi.org/10.1080/00794236.2025.2573248.
9. Afonso, L.V.; Varela Gomes, M.; Varela Gomes, R. Chinese pornography in a Portuguese nunnery: on a transition period blue and white porcelain bowl recovered from Santana Convent (Lisbon). *Antiquaries Journal*, **2023**, *11*, 315-332. https://doi.org/10.1017/S0003581523000318
10. Shanshan, L.; Varela Gomes, M.; Xiong, H.; Varela Gomes, R.; Gonçalves, J. Gilded and colourful at the Santana Convent table (Lisbon, Portugal), *Europa Post Mediaevalis*, **2024**, *4*, 229-240.
11. Ferraria, A.M.; Carapeto, A.P.; Botelho do Rego, A.M. X-ray photoelectron spectroscopy: silver salts revisited. *Vacuum* **2012**, *86*, 1988-1991. http://dx.doi.org/10.1016/j.vacuum.2012.05.031
12. Beamson, G.; Briggs, D. *High Resolution XPS of Organic Polymers, The Scienta ESCA300 Database*, Wiley, New York, 1992. https://doi.org/10.1002/adma.19930051035
13. Vieira Ferreira, L.F.; Machado, I.F.; Ferraria, A.M.; Casimiro, T.M.; Colomban, Ph. Portuguese tin-glazed earthenware from the 16th century: A spectroscopic characterization of pigments, glazes and pastes. *Appl. Surf. Sci.* **2013**, *285P*, 144–152. http://dx.doi.org/10.1016/j.apsusc.2013.08.016
14. Vieira Ferreira, L.F.; Casimiro, T.M.; Colomban, Ph. Portuguese tin-glazed earthenware from the 17th century. Part 1: Pigments and glazes, *Spectrochimica Acta A* **2013**, *104*, 437-444. http://dx.doi.org/10.1016/j.saa.2012.11.069
15. Vieira Ferreira, L.F.; Barros, L.; Machado, I.F.; Pereira, M.F.C.; Casimiro, T.M. An archaeometric study of a Late Neolithic cup and coeval and Chalcolithic ceramic sherds found in the São Paulo Cave, Almada, Portugal. *J. Raman Spectrosc.* **2020**, *52*, 483-492. https://doi.org/10.1002/jrs.5802
16. Vieira Ferreira, L.F.; Barros, L.; Machado, I.F.; Gonzalez, A.; Pereira, M.F.C.; Casimiro, T.M. Spectroscopic characterization of amphorae from the 8th to the 7th c. BCE found at the Almaraz settlement in Almada, Portugal. *J. Archaeol. Science: Reports* **2018**, *21*, 166-174. https://doi.org/10.1016/j.jasrep.2018.07.005

 doi:10.20944/preprints202605.1370.v1

17. Vieira Ferreira, L.F.; A. Gonzalez, A.; Pereira, M.F.C.; Santos, L.F.; Casimiro, T.M.; Ferreira, D.P.; Conceição, D.S.; Machado, I.F. Spectroscopy of 16th century Portuguese tin-glazed earthenware produced in the region of Lisbon. *Ceram. Int.* **2015**, *41*, 13433–13446. https://doi.org/10.1016/j.ceramint.2015.07.132
18. Colomban, Ph.; Kırmızı, B.; Simsek Franci G. Cobalt and Associated Impurities in Blue (and Green) Glass, Glaze and Enamel: Relationships between Raw Materials, Processing, Composition, Phases and International Trade. *Minerals* **2021**, *11*, 633 (42 pages). https://doi.org/10.3390/min11060633
19. Reiche, I.; Röhrs, S.; Salomon, J.; Kanngießer, B.; Höhn, Y.; Malzer, W.; Voigt, F. Development of a nondestructive method for underglaze painted tiles—demonstrated by the analysis of Persian objects from the nineteenth century, *Anal Bioanal Chem* **2009**, *393*, 1025–1041. https://doi.org/10.1007/s00216-008-2497-7
20. Edwards, H.; Colomban, Ph. Blue by Fire: A Marker of the Technical History of Glass and Ceramics, *in Cultural Heritage Science*, Springer. 2025. https://doi.org/10.1007/978-3-031-77122-4
21. Bellmann, A.; Rautenberg, C.; Bentrup U.; Brückner A. Determining the Location of Co^{2+} in Zeolites by UV-Vis Dffuse Reflection Spectroscopy: A Critical View. *Catalysts* **2020**, *10*, 123 (12 pages). https://doi.org/10.3390/catal10010123
22. Visinescu, D.; Paraschiv, C.; Ianculescu, A.; Jurca, B.; Vasile, B.; Carp, O. The environmentally benign synthesis of nanosized $Co_xZn_{1-x}Al_2O_4$ blue pigments. Dyes Pigment. **2010**, 87, 125–131. https://doi.org/10.1016/j.dyepig.2010.03.006
23. Naumkin, A.V.; Kraut-Vass, A.; Gaarenstroom, S.W.; Powell, C.J. *NIST X-ray Photoelectron Spectroscopy Database*, Version 5.0, https://dx.doi.org/10.18434/T4T88K. Accessed the 27th April 2026.
24. Biesinger, M.C.; Payne, B.P.; Grosvenor, A.P.; Lau, L.W.M.; Gerson, A.R.; Smart, R.St.C. Resolving surface chemical states in XPS analysis of first row transition metals, oxides and hydroxides: Cr, Mn, Fe, Co and Ni. *Appl. Surf. Sci.* **2011**, *257*, 2717-2730. http://dx.doi.org/10.1016/j.apsusc.2010.10.051.
25. Fantauzzi, M.; Secci, F.; Angotzi, M.S.; Passiu, C.; Cannas, C.; Rossi, A. Nanostructured spinel cobalt ferrites: Fe and Co chemical state, cation distribution and size effects by X-ray photoelectron spectroscopy, *RSC Adv.* **2019**, *9*, 19171-19179. https://doi.org/10.1039/C9RA03488A
26. Colomban, Ph.; Tournié, A.; Bellot-Gurlet, L. Raman identification of glassy silicates used in ceramics, glass and jewellery: a tentative differentiation guide, *J. Raman Spectrosc.* **2006**, *37*, 841-852. http://dx.doi.org/10.1002/jrs.1515
27. Colomban, Ph. On site Raman identification and dating of ancient glasses: a review of procedures and tools, J. Cult. Herit. 9 (2008) e55-e60. https://doi.org/10.1016/j.culher.2008.06.005
28. Colomban, Ph. Polymerization degree and Raman identification of ancient glasses used for jewelry, ceramic enamels and mosaics, *J Non-Crystalline Solids* **2003**, *323*, 180–187. http://dx.doi.org/10.1016/S0022-3093(03)00303-X
29. Vieira Ferreira, L.F.; Machado, I.F.; Casimiro, T.M.; Pereira, M.F.C.; Santos, L.F. Portuguese Blue-on-Blue 16th-17th c. Pottery, *Archaeometry* **2018**, *21*, 166-174, http://dx.doi.org/10.1111/arcm.12336
30. Wen, J.; Chen, Z.; Zeng, Q.; Hu, L.; Wang, B.; Shi, J.; Zhang, G. Multi-micro analytical studies of blue-and-white porcelain (Ming dynasty) excavated from Shuangchuan island, *Ceram. Int.* **2019**, *45*, 13362–13368. https://doi.org/10.1016/j.ceramint.2019.04.031
31. Wood, N. *Chinese Glazes: Their Origins, Chemistry, and Re-creation*. University of Pennsylvania Press, 1999, Philadelphia.
32. Yap, C.T.; Tang, S.M. X-Ray Fluorescence Analysis of Modern and Recent Chinese Porcelains, *Archaeometry* **1984**, *26*, 78-81. https://doi.org/10.1111/j.1475-4754.1984.tb00320.x
33. Yap, C.T. A Quantitative Spectrometric Analysis of Trace Concentrations of Manganese and Cobalt in Ceramics and the Significance of As/Co and Mn/Co Ratios, *J. Archaeological* Sci. **1988**, *15*, 173-177. https://doi.org/10.1016/0305-4403(88)90005-2
34. Kingery, W.D.; Bowen, H.K.; Uhlmann, D.R. *Introduction to Ceramics*, 2nd Edition, Wiley, New York, 1976.
35. Rice, P.M. *Pottery Analysis: A Sourcebook*, University of Chicago Press, Chicago, 1987.
36. Quinn, G.D. A History of the Fractography of Glasses and Ceramics. In *Fractography of Glasses and Ceramics VI: Ceramic Transactions*; Varner, J.R.; Wightman M., Eds. The American Ceramic Society. Book Series: Ceramic Transactions Series, Wiley, New Jersey, 2012, Chapt. 1, pp. 1-55. https://doi.org/10.1002/9781118433010.ch1

 doi:10.20944/preprints202605.1370.v1

37. Tite, M.S.; Freestone, I.; Mason, R.; Molera, J.; Vendrell-Saz, M.; Wood, N. Lead glazes in antiquity—methods of production and reasons for use. *Archaeometry* **1998**, *40*, 241-260. https://doi.org/10.1111/j.1475-4754.1998.tb00836.x
38. Vandiver, P.B., The role of materials research in the study of ancient ceramics, *Annu. Rev. Mater. Res.* **2001**, *31*, 373–385.